


Two-dimensional crystalline platinum oxide

Received: 5 January 2024

Accepted: 19 August 2024

Published online: 19 September 2024

 Check for updates

Jun Cai ^{1,2,7}, Liyang Wei^{1,7}, Jian Liu ^{2,7}, Chaowu Xue^{1,7}, Zhaoxi Chen², Yuxiong Hu¹, Yijing Zang ², Meixiao Wang², Wujun Shi ², Tian Qin³, Hui Zhang⁴, Liwei Chen ³, Xi Liu ³, Marc-Georg Willinger ⁵, Peijun Hu^{1,2}, Kaihui Liu ⁶, Bo Yang ¹✉, Zhongkai Liu ¹✉, Zhi Liu ^{1,2}✉ & Zhu-Jun Wang ^{1,2}✉

Platinum (Pt) oxides are vital catalysts in numerous reactions, but research indicates that they decompose at high temperatures, limiting their use in high-temperature applications. In this study, we identify a two-dimensional (2D) crystalline Pt oxide with remarkable thermal stability (1,200 K under nitrogen dioxide) using a suite of in situ methods. This 2D Pt oxide, characterized by a honeycomb lattice of Pt atoms encased between dual oxygen layers forming a six-pointed star structure, exhibits minimized in-plane stress and enhanced vertical bonding due to its unique structure, as revealed by theoretical simulations. These features contribute to its high thermal stability. Multiscale in situ observations trace the formation of this 2D Pt oxide from α -PtO₂, providing insights into its formation mechanism from the atomic to the millimetre scale. This 2D Pt oxide with outstanding thermal stability and distinct surface electronic structure subverts the previously held notion that Pt oxides do not exist at high temperatures and can also present unique catalytic capabilities. This work expands our understanding of Pt oxidation species and sheds light on the oxidative and catalytic behaviours of Pt oxide in high-temperature settings.

In a range of industrial applications, platinum (Pt) is subject to oxidation under demanding conditions, including exposure to oxidizing atmospheres and high temperatures. Therefore, a thorough understanding of the oxidation behaviour of Pt is essential to optimize the efficiency and longevity of catalysts¹. This process plays a vital role in various heterogeneous reactions such as CO/NO_x oxidation (three-way catalysts)², ammonia oxidation³, fuel cell operations⁴ and electrochemical oxygen reduction^{5–7}. Understanding the formation and characteristics of Pt oxides is essential, as they significantly influence the reactivity of Pt-based catalysts in these diverse reactions and are central to the efficiency and functionality of Pt-based catalysts^{8–11}.

A multitude of preceding investigations have examined the oxidation phenomena of Pt, probing diverse conditions encompassing exposure to oxygen, ozone and nitrogen dioxide^{12–18}. Such studies, often conducted via traditional surface science techniques under ultrahigh-vacuum (UHV) conditions, revealed that at 300 K, the Pt(111) surface becomes cloaked with a layer of adsorbed oxygen atoms, attaining coverage levels up to 0.25 monolayer (ML) in a p(2 × 2)-O configuration¹⁹. Using atomic oxygen sources, such as ozone or nitrogen dioxide, facilitates achieving higher oxygen coverage on Pt surfaces. In particular, the interaction of NO₂ with Pt(111) at 450 K has been observed to induce the formation of 0.75 ML of chemisorbed oxygen¹⁵, whereas

¹School of Physical Science and Technology & Shanghai Key Laboratory of High-resolution Electron Microscopy, ShanghaiTech University, Shanghai, China. ²Center for Transformative Science, ShanghaiTech University, Shanghai, China. ³In-situ Center for Physical Sciences, School of Chemistry and Chemical Engineering, Shanghai Jiao Tong University, Shanghai, China. ⁴Shanghai Synchrotron Radiation Facility, Shanghai Advanced Research Institute, Chinese Academy of Sciences, Shanghai, China. ⁵Technical University of Munich, Chair of Electron Microscopy, Garching, Germany. ⁶State Key Laboratory for Mesoscopic Physics, Frontiers Science Centre for Nano-optoelectronics, School of Physics, Peking University, Beijing, China. ⁷These authors contributed equally: Jun Cai, Liyang Wei, Jian Liu, Chaowu Xue. ✉e-mail: yangbo1@shanghaitech.edu.cn; liuzhk@shanghaitech.edu.cn; liuzhi@shanghaitech.edu.cn; wangzhj3@shanghaitech.edu.cn

ozone at 300 K can elevate the oxygen coverage to as much as 2.4 ML (ref. 13). When subjected to high temperatures and high pressures, Pt surfaces exhibit various morphologies, including one-dimensional oxidic rows, triangular oxides and the more unstable α -PtO₂ (refs. 14,16,17,20). The detailed Pt–O phase diagram is shown in Supplementary Note 1. Despite extensive research efforts, the dynamic evolution and structural intricacies of various Pt oxide species remain enveloped in a veil of scientific ambiguity^{21–25}.

Understanding the oxidation of Pt requires examining the structural and electronic changes at atomic resolution during oxidation processes in realistic reaction conditions²⁶. By using a comprehensive suite of in situ real-space instruments, we observe the transformation of surface oxides across scales—from atomic to millimetre—bridging the pressure gap between UHV and practical environments²⁷. This approach integrates localized atomistic structures from in situ scanning tunnelling microscopy (STM) and transmission electron microscopy (SEM)^{27–30}. The combined use of in situ imaging and ambient-pressure X-ray photoelectron spectroscopy (AP-XPS) enables us to correlate detailed atomic structures with macroscopic transformation dynamics under dynamic, non-equilibrium conditions^{31–33}. We investigate the oxidation of Pt(111) under a NO₂ atmosphere from room temperature to 1,000 K with various levels of increase. Our findings indicate that at temperatures below approximately 700 K, the Pt(111) surface is enveloped by amorphous α -PtO₂. However, α -PtO₂ demonstrates instability at temperatures exceeding 750 K, undergoing a transition into an oxide phase. Using a combination of complementary in situ methods, we characterize the surface structure of this oxide. Our integrated approach indicates that the observed Pt oxide forms a honeycomb lattice of Pt atoms sandwiched between dual oxygen layers, creating a distinct out-of-plane six-pointed star structure. It exhibits two-dimensional (2D) crystalline properties and exceptional thermal stability above 750 K. Further in situ SEM and AP-XPS observations reveal that this 2D Pt oxide retains its integrity even at 1,200 K. Such observed exceptional thermal stability challenges the prevailing understanding that the structure of Pt oxides becomes unstable above 700 K (refs. 34,35). Comprehensive theoretical analysis, including density functional theory (DFT) and molecular dynamics (MD) simulations with a machine learning force field, accurately describes the surface structure and confirms the stability of this oxide at the atomic level under various conditions.

Besides remarkable thermal stability, this 2D crystalline Pt oxide also presents a unique surface electronic structure, facilitating the selective oxidation of CO in environments containing a mixture of methane, oxygen and CO. Furthermore, the Pt oxide formed in the presence of NO₂ can also be produced under other oxidizing conditions. This research enhances our knowledge of Pt oxidation species and provides an insight into the behaviour of Pt oxide in terms of oxidation and catalysis, particularly in high-temperature and oxidizing settings. These findings have important implications for the design and development of advanced catalysts. In particular, the outstanding thermal stability under oxidative duress indicates that this 2D Pt oxide may represent the primary active phase of Pt in such environments, a revelation that redefines the understanding of the role of Pt oxide in catalysis.

Results and discussion

Observing the oxidation of Pt

The surface oxide was grown by annealing the Pt(111) substrate in the presence of 1 mbar NO₂ at 1,000 K. The Pt(111) surface was cleaned by cycles of sputtering and annealing in advance (Supplementary Note 2). In situ SEM images (Fig. 1a) captured the oxidation process of Pt. The homogeneously grey level increasing in the secondary-electron image reflects the changes in the surface work function during NO₂ oxidation (Fig. 1b and Supplementary Video 1). Therefore, the in situ

SEM observations imply the formation of uniform layered species on the Pt(111) surface under a NO₂ atmosphere at 1,000 K.

To identify these surface processes, the chemical state of the surface species was monitored by AP-XPS to fingerprint the composition and evolution behaviour of surface species. Figure 1c and Supplementary Video 2 show the evolution of O1s spectra gathered under NO₂ conditions from 300 to 1,000 K, and the fitted spectra are shown in Supplementary Fig. 3. Initially, the surface was covered with adsorbed NO* (531.6 eV) and chemisorbed oxygen atoms (529.8 eV) from room temperature to 450 K (refs. 36,37). As the temperature increased, PtO₂ gradually formed, as evidenced by the O1s peak (530.4 eV) and Pt4f_{5/2} peak (72.0 eV) (Supplementary Fig. 3 and Fig. 1c)^{16,36,38}. Similar PtO₂ formation processes have been observed under oxygen or ozone conditions^{12,13}.

By further increasing to 1,000 K, an oxygen-containing species emerged, as depicted by the O1s peak at approximately 531.5 eV (Fig. 1c and Supplementary Fig. 3). The change in peak intensity (Fig. 1c) at higher temperatures could be attributed to the thermal expansion of the sample holder (Supplementary Note 3 and Supplementary Video 3). The depth profile shown in Fig. 1d indicates that the oxide species formed on this surface (Supplementary Note 4). In particular, the Pt(111) surface displayed neither N nor other contaminations (Supplementary Fig. 7). Hence, the surface species consists of Pt and O with a ratio of approximately 1 to 2.7 (Pt/O) (Supplementary Note 5). Thus, we temporarily assigned the surface thin film as PtO_x. Considering that the experimental conditions between in situ SEM and AP-XPS were identical, we can correlate the evolution of the electronic structure of PtO_x with the uniform secondary-electron contrast change of the Pt surface recognized by SEM observations.

To further elucidate the chemical properties of PtO_x, the evolution of the O1s spectra was monitored during reduction by simply switching from NO₂ to hydrogen. The O1s spectra under 0.1 mbar H₂ at 1,000 K show the reduction process of the PtO_x film (Fig. 2a). The intensity of the O1s peak decreased slowly and required approximately 60 min to disappear entirely. The in situ SEM provides real-space details of the surface reduction processes. As shown in Fig. 2b, the area with a high grey level (high intensity) in the SEM image corresponds to the regions covered by PtO_x, whereas the low-grey-level (low-intensity) areas represent the bare Pt surface (vacancy island). The formation of aligned vacancy islands with similar triangular shapes emerged and expanded over time during exposure to the H₂ atmosphere. When neighbouring aligned vacancy islands met, the contact region exhibited a sharp concave corner and gradually became roundish with time (Fig. 2b, red arrows). The propagation of the roundish concave corners expanded rapidly and replaced the original smooth edges (Fig. 2c and Supplementary Video 4). Such an evolution behaviour is a signature of the inherent seamless coalescence behaviour of a 2D crystalline film²⁷. This observation implies that the chemical configuration of PtO_x reveals a highly 2D crystalline film, and provides an indirect indication that the PtO_x overlayer could even be a single-crystalline film.

Additionally, we analysed the shape of the vacancy islands to validate this crystalline nature. Under the assumption that PtO_x is a 2D crystalline film, the triangular shape of the vacancy island should be related to the crystallographic orientation of the Pt grain. The spatial and angular distributions of crystallographic orientations (9 10 7) are clearly visualized by electron backscatter diffraction (EBSD) observation in the Pt cubic cell (Fig. 2d,e). The corresponding surface atomic structure can be deduced³⁹. The surface of Pt(9 10 7) exhibits a distinct terrace–step–kink structure in the ideal state (Fig. 2f). Because the surface step and kink play a key role in the nucleation of a 2D crystal and define the in-plane orientation of the overlayer^{40,41}, the observed orientations of the vacancy islands should correlate with the atomic structure of the (9 10 7) surface. The shape of the vacancy island almost perfectly overlaps with the triangle surrounded by stripes along [1 0 -1], [0 1 -1] and the line along the (9 10 7) surface step (Fig. 2g), signifying that the PtO_x film underwent epitaxial growth on the (9 10 7) surface⁴².

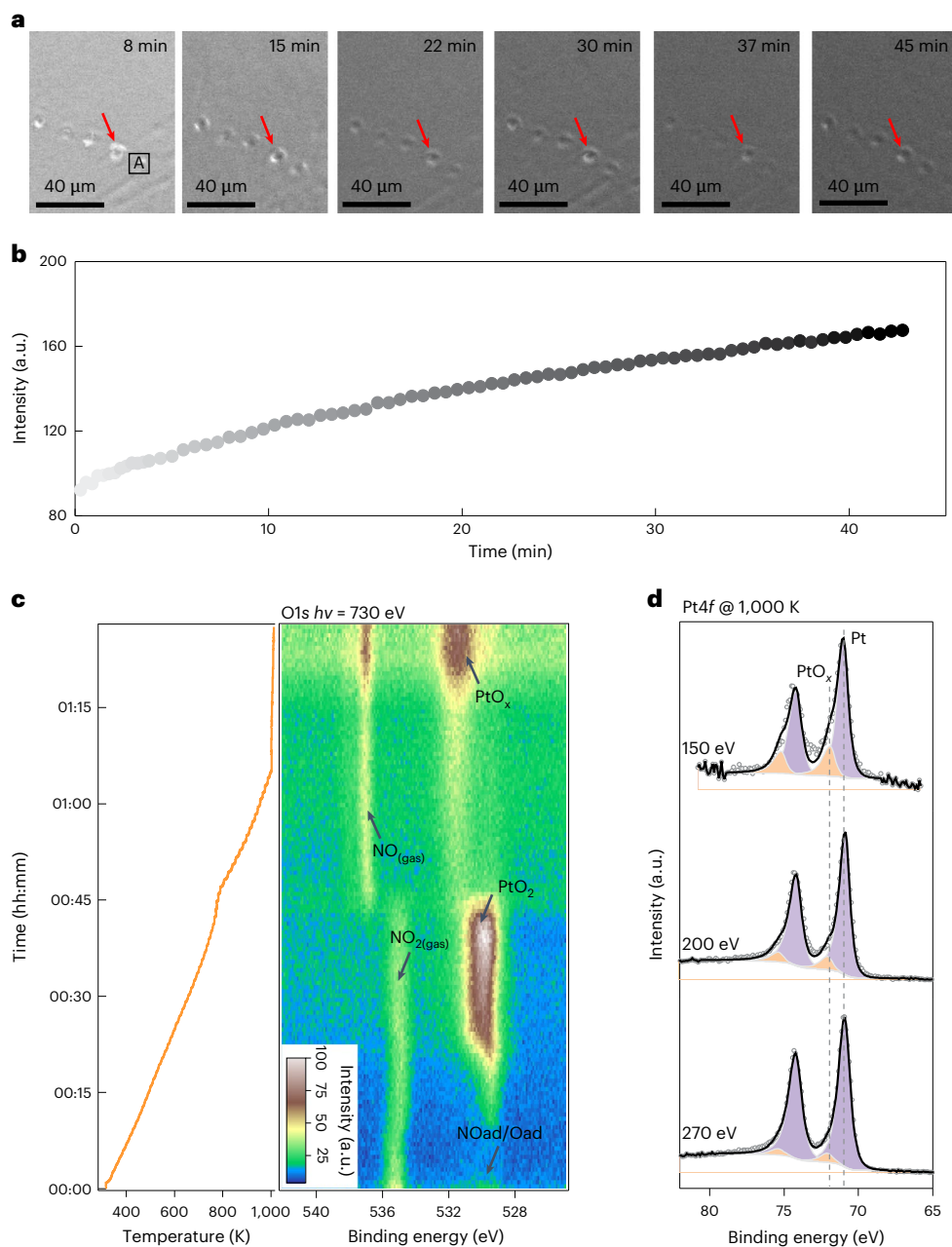


Fig. 1 | Formation of PtO_x layer on Pt(111) under NO_2 . **a**, In situ SEM images obtained during the oxidation of Pt(111) by 1 mbar NO_2 under 1,000 K. **b**, Change in intensity in region A (shown in **a**). **c**, Evolution of the O1s spectra during the oxidation process on a Pt(111) surface under 1 mbar NO_2 from 300 to 1,000 K.

d, Pt4f spectra of the PtO_x collected with various photon energies, demonstrating that PtO_x was located at the topmost surface. The red arrows indicate identical positions on the Pt surface. A complete oxidation process is shown in Supplementary Videos 1 and 2.

Moreover, the individual vacancy islands grew self-similarly in the shape of a truncated equilateral triangle (Fig. 2h,i), indicating that each vacancy island was co-oriented and similarly attached to a Pt surface step⁴³. Thus, the substrate structure and associated barriers along and across the steps led to an in-plane anisotropic evolution (Fig. 2j). To rationalize the experimental observations, we performed kinetic Wulff construction simulations of the vacancy island shapes during etching based on the experimentally obtained anisotropic evolution rates. The relative expansion rates along different directions were obtained by measuring the distances from the position of the initial etching to the respective edge (Fig. 2j, green arrows). Only the expansion speed of the edges was utilized as the parameter for simulating anisotropic evolution. The resulting polar plots of the orientation-dependent expansion rates are exhibited in Fig. 2k.

The striking consistency between the experimental observation and simulated evolution further validates our proposed model in which the PtO_x overlayer is 2D single crystalline.

Characterization of the platinum oxide lattice constant

Thus far, by using spatially resolved and time-resolved observations, we have confirmed that the etching behaviours of PtO_x share the characteristic features of a 2D crystalline material. To pinpoint the atomic structure and chemical configuration of the PtO_x film, we now turn to reciprocal space by using low-energy electron diffraction (LEED) to predict the possible atomic structure of PtO_x (refs. 44,45).

LEED measurements reveal a set of six outermost spots originating from the Pt(111) substrate (Fig. 3a, green dashed rhombus labelled β), and another set of six spots arising from the PtO_x film (Fig. 3a, bright

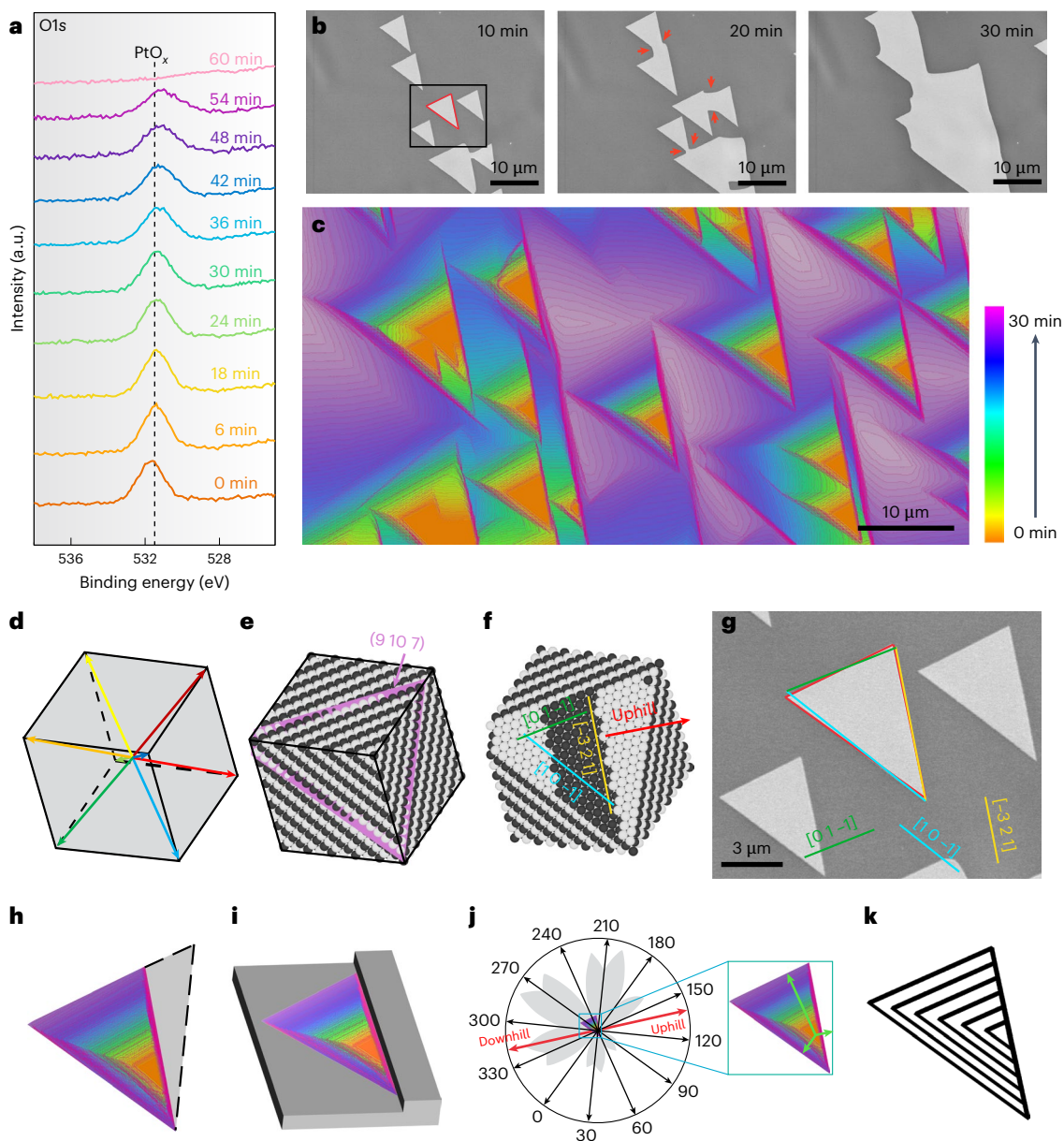


Fig. 2 | H₂ etching process of a PtO_x layer. a, Evolution of the O1s spectra of PtO_x under 1 mbar H₂ at 1,000 K; the spectra were collected under a photon energy of 1,486.6 eV. **b**, In situ SEM images recorded the etching behaviour of PtO_x on a Pt(9 10 7) surface showing anisotropic evolution under 1 mbar H₂ at 1,000 K (Supplementary Video 3). Note: the sequence of images shows the appearance of new edges at the concave corner during the coalescence of etching pits (highlighted by red arrows). **c**, Shape evolution of the etching pits during H₂ etching, reproduced as the colour-coded superposition of outlines abstracted from images recorded at 53 s intervals. **d**, Orientation of the Pt substrate is determined by EBSD and presented in the Pt unit cell. The coloured arrows indicate the <111> directions for the unit cell. **e**, The corresponding ball model. **f**, Ball model of the unreconstructed (9 10 7) surface orientation of the

underlying Pt grain. The yellow line highlights the surface step, with the uphill direction indicated by the red labelled arrow. **g**, Representative details of the vacancy islands (etching pits) in **b**. The shape of the vacancy islands almost perfectly overlaps the triangle surrounded by the stripes along [1 0 -1], [0 1 -1] and the line along the (9 10 7) surface step. **h**, Colour-coded shape evolution of an etching pit according to the growth time provided in the colour legend. The black dotted line indicates the missing half of the regular triangle shape. **i**, Schematic of the attachment of one of the vacancy island edges to the Pt step site. **j**, Shape evolution of the etching pits represented in polar coordinates shows anisotropic growth behaviour. Note: the initiation site of the etching pits is from the pole of the polar coordinates. **k**, Simulated kinetic Wulff construction of growth.

blue dashed rhombus labelled α). Additionally, the LEED observations across diverse energy ranges and spatial extents confirm that the as-grown PtO_x exhibits high crystallinity, manifesting as a large-area, 2D single-crystalline film (Supplementary Figs. 8 and 9 and Supplementary Video 5). There is a discernible relative rotation angle of 30° between the PtO_x film and the underlying Pt(111) substrate (Supplementary Fig. 10). The moiré superlattice formed between PtO_x and Pt(111) appears as a series of satellite points surrounding six PtO_x spots (Fig. 3a), which are rotated by 30° with respect to the Pt(111) lattice

(Fig. 3b (red dashed rhombus) and Supplementary Fig. 10). The single set of LEED points for both PtO_x and the corresponding moiré pattern indicate strong interactions between the PtO_x film and the substrate^{27,46}. The LEED patterns reveal that the crystal lattice ratio of the PtO_x-Pt(111) system in reciprocal space is $\alpha:\beta:\gamma = 0.53:1:0.077$, corresponding to a proportional lattice ratio of $\alpha:\beta:\gamma = 1:0.53:6.9$ in real space. By utilizing the known crystal lattice constant of Pt(111), we can determine that the surface lattice for PtO_x is $\alpha = 0.53$ nm, and the moiré period for PtO_x on Pt(111) in real space is $\gamma = 3.65$ nm. Surprisingly, the lattice

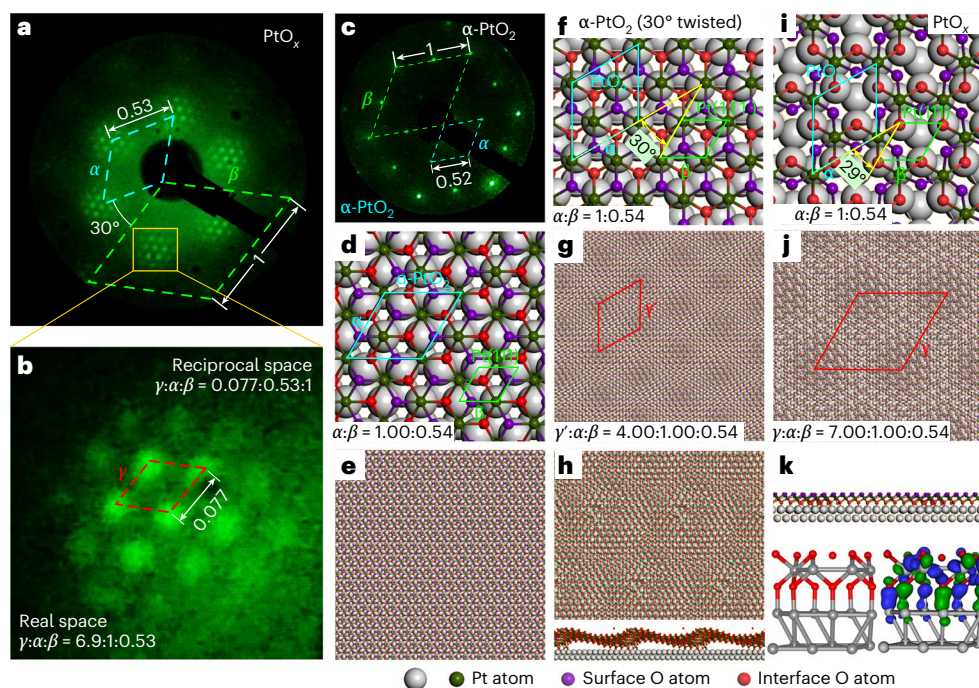


Fig. 3 | Characterization of the PtO_x layer. **a**, LEED pattern of the surface covered with a PtO_x layer. **b**, Enlarged image of the region in the yellow box in **a**. **c**, LEED pattern of the $\alpha\text{-PtO}_2$ overlayer on the Pt(111) surface. **d, e**, Schematic of the models for the $\alpha\text{-PtO}_2$ overlayer on Pt(111). **f, g**, Atomic model of the predicted structure of the PtO_x film (30°-rotated $\alpha\text{-PtO}_2$). **h**, MD simulation of the stability

of the rotated $\alpha\text{-PtO}_2$. **i**, Atomic structure after removing a Pt atom from the 30°-rotated $\alpha\text{-PtO}_2$. **j**, Formation of moiré pattern after structural relaxation. **k**, Cross-sectional view of the relaxed structure in **j**, depicting the interfacial bonding interactions between Pt and O.

constant of PtO_x closely resembles that of $\alpha\text{-PtO}_2$ (Fig. 3c–e), which aligns with the Pt(111) surface without rotation⁴⁷. We, thus, attempt to construct an atomic model for PtO_x by directly rotating $\alpha\text{-PtO}_2$ by 30° on Pt(111) (Fig. 3f). This rotation operation results in a moiré superstructure rotated by 30° with respect to Pt(111). In particular, this moiré superstructure measures 2.07 nm (Fig. 3g), which does not match our LEED observations. Furthermore, the MD simulations demonstrate that the surface atomic arrangement of a 30°-rotated $\alpha\text{-PtO}_2$ is thermodynamically unstable and prone to corrugation due to in-plane stress; such a surface arrangement cannot exist specially at relevant high temperatures (Fig. 3h, Supplementary Fig. 11 and Supplementary Videos 6 and 7).

To satisfy the diffraction pattern in reciprocal space and thermodynamic stability, reconstructing the surface atomic arrangement by periodically removing a Pt atom from the 30°-rotated $\alpha\text{-PtO}_2$ is necessary (Fig. 3i). The resulting reconstructed structure exhibits similarities to layered CrI_3 (ref. 48). This approach allows for the preservation of the lattice constant of $\alpha\text{-PtO}_2$ and achieve perfect matching with LEED observations in terms of in-plane rotation and moiré superstructure on Pt(111) (Fig. 3b, j). MD simulations indicate that this structural configuration helps release the in-plane stress and flatten the oxide overlayer (Fig. 3k, Supplementary Figs. 12 and 13 and Supplementary Videos 8 and 9)⁴⁹. In particular, within each vacancy created by removing a Pt atom, lower-layer O atoms form strong bonds with metallic Pt atoms located above them (Supplementary Note 6). We, thus, revise the chemical formula of PtO_x to be $\text{PtO}_3\text{-Pt}$. This Pt oxide exhibits a honeycomb lattice configuration, where Pt atoms are sandwiched between dual layers of O atoms, resulting in a distinctive six-pointed star structure when viewed from out of plane.

Imaging of the Pt oxide structure in real space

To corroborate the geometric inferences drawn from the LEED observations in reciprocal space, we undertook STM measurements to directly visualize the structure of $\text{PtO}_3\text{-Pt}$ in the real-space atomic level.

Figure 4a displays the STM topography of the pristine Pt(111) surface with large and flat terraces, showing the excellent quality of the substrate. On oxidation under 1 mbar NO_2 at 1,000 K, our STM topography reveals that the $\text{PtO}_3\text{-Pt}$ film is fully covered on the Pt(111) surface (Fig. 4b), where remarkable hexagonal moiré patterns are observed. Both the surface structure of $\text{PtO}_3\text{-Pt}$ with a lattice constant of 0.54 nm and the periodicity of the moiré patterns of 3.67 nm relative to Pt(111) are measured from the STM atomic-resolution images (Fig. 4c (rhombus) and Supplementary Fig. 14). Our STM results are close to our LEED observations (Fig. 4a, b (insets) and Fig. 3a, b), which reveal a lattice constant of 0.53 nm for $\text{PtO}_3\text{-Pt}$ and a period of 3.54 nm for the moiré superstructure (Supplementary Fig. 14).

Furthermore, our STM topography is fully consistent with the purposed six-pointed star structure of $\text{PtO}_3\text{-Pt}$ mentioned above. The dark spots in the topographic image (Fig. 4c, e) result from the absence of Pt atoms on the surface, and then we can directly superimpose the purposed structure of $\text{PtO}_3\text{-Pt}$ onto our STM image (Fig. 4c, right). Figure 4e shows the cropped image of the area highlighted by the white square in Fig. 4c. Both unit cells of the dark spots corresponding to the absence of a Pt atom and the period of the moiré patterns fit well with our purposed structure of $\text{PtO}_3\text{-Pt}$ and the corresponding theoretical simulation results (Fig. 4d, f).

Besides, the brightest spots are not directly above the surface O in both experimental and simulated STM images (Fig. 3g, j), suggesting a position offset of surface O, which can be understood by analysing the projected density of states from the side view (Fig. 4e). Figure 4e illustrates the schematic of the models and the corresponding electron density isosurfaces of the *p* orbitals of surface O, which exhibit a fusiform shape when viewed from the side (Fig. 4e, green line). The relative position of the scanning tip and its interaction with the isosurface along the scanning line demonstrates that the region with the highest electron density is not directly above the surface O atom, consistent with our experimental observations (Supplementary Videos 10 and 11). Consequently, by the combination of

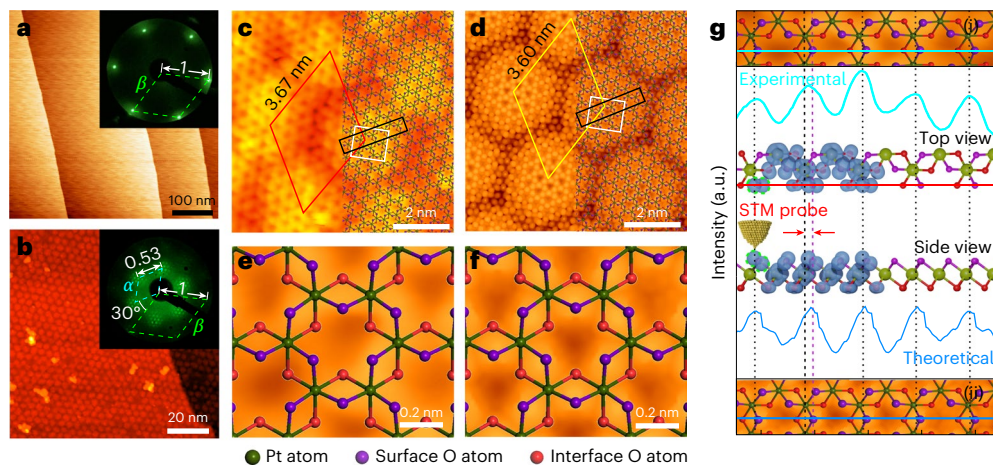


Fig. 4 | Real-space image of the PtO_3 -Pt structure. **a, b**, STM images of the clean Pt(111) surface (**a**) and the fully covered PtO_3 -Pt layer (**b**). The insets in **a** and **b** are the corresponding LEED patterns. **c**, Atomic-resolution STM images of the PtO_3 -Pt layer. **d**, Simulated STM image of the PtO_3 -Pt layer based on the structure shown in Fig. 3j. **e, f**, Enlarged image of the white box in **c** (**e**) and **d** (**f**). **g**, The top and bottom panels show the enlarged image of the black box in **c** and **d**, respectively; the line profile is a comparison between the experimental (along

the green line in **g**(i)) and theoretical (along the blue line in **g**(ii)) results; the middle panel is the electron density isosurface map from the top and side views. The LEED patterns were collected under the same energy (48 eV) and followed the same direction. Size and tunnelling parameters: **(a)** 500 nm \times 500 nm, $V_s = 50$ mV, $I = 1$ nA; **(b)** 100 nm \times 100 nm, $V_s = 1.74$ V, $I = 0.07$ nA; **(c)** 9.5 nm \times 9.5 nm, $V_s = 1.06$ V, $I = 0.07$ nA.

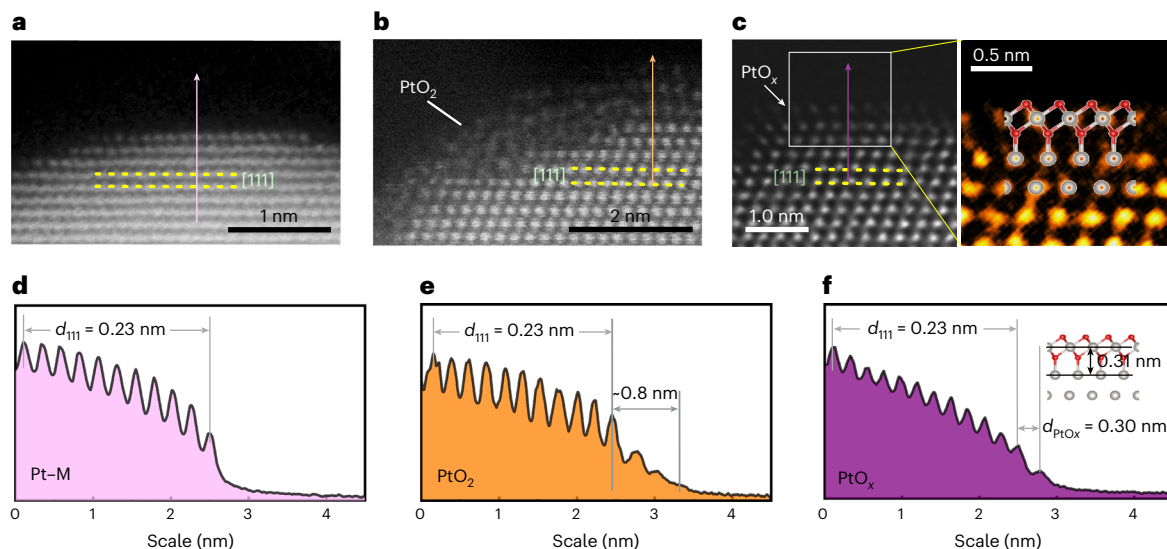


Fig. 5 | Direct observation of Pt oxidation by in situ STEM. **a–c**, STEM images of Pt nanoparticles under NO_2 at 300 K (**a**), 620 K (**b**) and 1,000 K (**c**). The right panel in **c** is a magnified image of the grey-box area (**c**, left) together with a superimposed PtO_3 -Pt model. **d–f**, Intensity profiles of the arrow-marked regions in **a** (**d**), **b** (**e**) and **c** (**f**).

experiments and theoretical simulations, we can clearly demonstrate that the spatial distribution of the p orbitals of surface O results from the observed positional offset of surface O atoms in the STM image (Fig. 4e, red arrows).

The core-level shift of the O1s spectra for the PtO_3 -Pt structure was also calculated (Supplementary Fig. 15). The result shows that the core-level shift of upper-layer O is lowered by about 1.01 eV compared with the lower-layer O, which is close to the experimental value of 1.29 eV. Furthermore, the number of the two forms of O atoms is the same with those in the atomic model, suggesting that the peak area of these two O1s peaks would be nearly equal. This is also consistent with the experimental results, showing that the peak area ratio of $\text{O}_{\text{int}}/\text{O}_{\text{surf}}$ is close to 1. For the valence state of Pt oxide, we calculated the Bader charges of PtO_3 -Pt and bulk α - PtO_2 systems. The results show that the valence state of Pt in PtO_3 (-Pt) should be slightly higher than +4 (Supplementary Note 7).

Until now, we have elucidated the structure of 2D layered PtO_3 -Pt and gained insights into the influence of the interaction between the six-pointed star overlayer and the substrate on this structure. To further investigate the spatial structure of PtO_3 -Pt, we used in situ scanning transmission electron microscopy (STEM) for operando cross-sectional imaging, capturing the growth process of PtO_3 -Pt in a NO_2 atmosphere.

Figure 5a–c illustrates the evolution behaviour of surface Pt oxides on the (111) plane from an out-of-plane perspective under 300, 620 and 1,000 K, respectively. As a reference, a high-angle annular dark-field STEM image of a Pt nanoparticle obtained at 300 K is demonstrated in the cleaned Pt(111) plane (Fig. 5a). The interspacing of the (111) plane is demonstrated in the cleaned Pt(111) plane (Fig. 5d). Increasing the temperature led to the distinct oxidation states of the Pt particle. Within the temperature range of 500–700 K, a disordered oxide with a thickness of several atomic layers is developed on Pt (Fig. 5b), and this structure is assigned to α - PtO_2 (refs. 50–52).

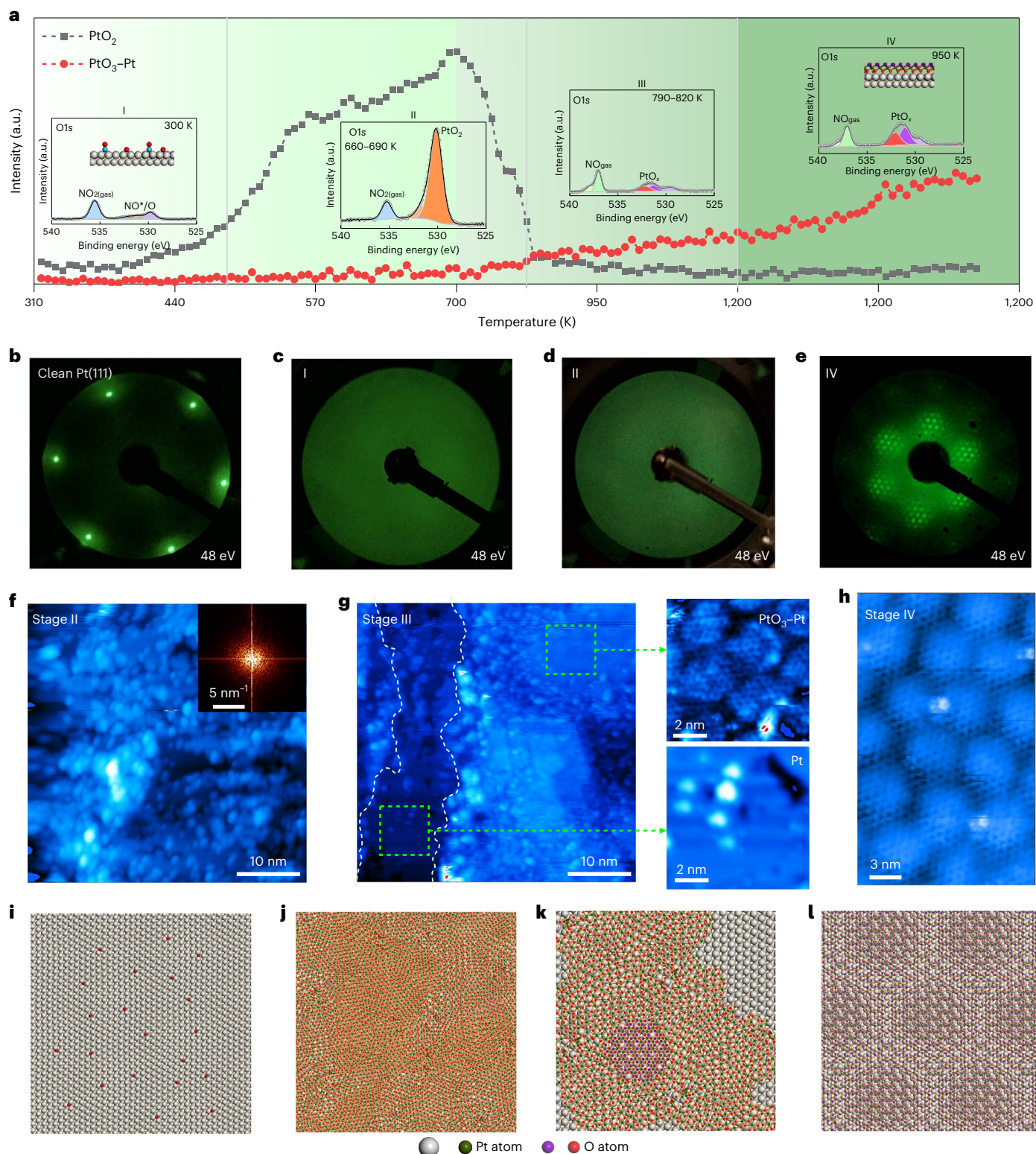


Fig. 6 | Evolution process from Pt to PtO₃-Pt. **a**, O1s peak area evolution of PtO₂ and PtO₃-Pt in Fig. 1c as a function of temperature. The insets show the O1s spectra under different stages. **b**, LEED pattern of the clean Pt(111) surface. **c-e**, Corresponding LEED patterns at stage I (**c**), stage II (**d**) and stage IV (**e**).

f,g, STM images collected at stage II (**f**) and stage III (**g**) in **a**. **i-l**, Atomic models during the oxidation process. Tunnelling parameters: (**f**) $V_s = 500$ mV, $I = 0.14$ nA; (**g**) $V_s = 1.5$ V, $I = 0.21$ nA; (**g**(i)) $V_s = 1.5$ V, $I = 0.21$ nA; (**g**(ii)) $V_s = 1.5$ V, $I = 0.21$ nA; (**h**) $V_s = 2.6$ V, $I = 0.18$ nA.

The profile of the contrast plot along the cross section shows that the thickness of α -PtO₂ is ~ 0.8 nm (Fig. 5e). With additional annealing up to 1,000 K, the gas-solid interface underwent a transformation, resulting in a monolayer oxide (Fig. 5c and Supplementary Fig. 17). This

oxide layer is positioned 0.30 nm away from the (111) plane (Fig. 5f). The electron energy loss spectroscopy (EELS) analysis (Supplementary Fig. 18) confirms the formation of an oxide layer on the Pt surface. An atomically resolved monolayer oxide together with the atomic model

structure of PtO₃-Pt is proposed from previous STM observations (Fig. 5c). The in situ STEM imaging of Pt(111) oxidation processes under NO₂ reveals the disordered α-PtO₂ layer in the transition state during PtO₃-Pt formation.

Mechanism of PtO₃-Pt formation

To further understand the layered PtO₃-Pt formation, we compare the in situ LEED, STEM and AP-XPS observations across the entire oxidation process. The in situ LEED observations of the Pt(111) oxidation process under conditions identical to the above STEM experiments are shown in Fig. 6c–e, starting from the clean Pt(111) surface (Fig. 6b). The LEED patterns of the Pt(111) substrate gradually become blurred and diffused with increasing temperature (Fig. 6c,d). This observation implies that the surface structure became disordered, consistent with the previous in situ STEM measurement (Fig. 5b). With further annealing to 1,000 K, the disordered surface converted to a well-ordered structure (Fig. 6e), agreeing with the in situ STEM visualizations (Fig. 5c). The corresponding evolution of the O1s spectra at different oxidation stages is presented in Fig. 6a (insets). Therefore, the in situ AP-XPS experiments prove that the comparison between in situ STEM/LEED and in situ environmental scanning electron microscopy (ESEM) is legitimate. In particular, the evolution of the O1s spectra indicates a rapid disappearance of α-PtO₂ at the inception of PtO₃-Pt growth. Nonetheless, at this juncture, we remain limited in our ability to elucidate the detailed transition from α-PtO₂ to PtO₃-Pt on an atomic scale, which constrains our comprehensive understanding of the formation processes. Therefore, we used quasi-in situ STM to capture the atomic structure of the surface at various oxidation stages, guided by the AP-XPS findings (see the ‘Quasi-in situ STM’ section). The quasi-in situ STM observations reveal that at the stage of α-PtO₂ formation, the surface displays a disordered structure (Fig. 6f). This observation aligns well with the in situ STEM data (Fig. 5b).

As the temperature went to 700 K, α-PtO₂ began to desorb from the Pt(111) surface, leading to the appearance of the O1s spectra of PtO₃-Pt (Fig. 6a, stage III). Subsequent quasi-in situ STM observations revealed a surface with intricate topographic features (Fig. 6g), characterized by the coexistence of flat areas and undulating regions attributed to α-PtO₂. On detailed examination, these flat areas were categorized into two distinct types: plain and plateau. High-resolution STM measurements confirmed that the plain areas represent the unaltered Pt(111) surface (Fig. 6g), whereas the plateau regions correspond to areas covered by PtO₃-Pt, displaying the characteristic moiré corrugation due to the overlayer-Pt(111) interaction. The simultaneous presence of α-PtO₂ and PtO₃-Pt suggests that PtO₃-Pt evolves from α-PtO₂ (the atomic model of the PtO₃-Pt evolution process is shown in Fig. 6i–l), rather than forming directly on the pristine Pt(111) surface.

Thermodynamic stability of PtO₃-Pt

To understand the thermodynamic stability of PtO₃-Pt on the Pt(111) substrate, the free energy changes (Δ*G*) associated with oxidizing the Pt(111) surface by O₂ or NO₂ to form either a single-layer PtO₃/Pt or α-PtO₂/Pt system were further investigated by DFT calculations. The results shown in Supplementary Fig. 19 suggest that under the investigated conditions of temperature from 300 to 1,300 K and 1 mbar O₂ or NO₂, the Δ*G* value of all the oxidation processes is always negative. This indicates that all the oxidation processes are thermodynamically favourable.

The formation of 2D PtO₃-Pt (PtO_x) structures under O₂ conditions requires relatively elevated temperatures, as demonstrated in Supplementary Note 8. To assess the stability of PtO₃-Pt formed in O₂ and NO₂ environments, we pumped out the oxygen as the sample was held at 1,300 K. After the sample was cooled under UHV, the X-ray photoelectron spectroscopy (XPS) spectra and LEED patterns were obtained to identify the PtO₃-Pt species (Supplementary Fig. 21). Comparing them with those formed under NO₂ conditions, we conclude that the

2D structure of PtO₃-Pt is stable under both O₂ and NO₂ conditions, even in UHV, at elevated temperatures.

The transition from α-PtO₂ to PtO₃-Pt on heating can be ascribed to the weaker affinity of α-PtO₂ for the Pt substrate than PtO₃-Pt (Supplementary Note 9). Due to the instability of α-PtO₂ oxides, which readily sublimate from the Pt surface^{35,53}, metallic Pt typically exhibits linear rates of weight loss in oxidizing atmospheres, forming volatile oxides at high temperatures (Supplementary Fig. 22). However, our findings reveal that the six-pointed star structure of Pt oxide exhibits exceptional thermodynamic stability, enduring even at temperatures as high as 1,200 K. Consequently, this 2D crystalline PtO₃-Pt serves as a protective layer, which was very similar to the 2D rafts of PdO_x (refs. 54,55), effectively shielding the substrate from continuous oxidation and sublimation (Supplementary Fig. 22).

Conclusion

In summary, our comprehensive study of Pt(111) oxidation under NO₂ conditions, covering temperatures from room temperature to 1,000 K, reveals that the Pt(111) surface was initially covered with adsorbed oxygen and NO* species. As the temperature increased, an amorphous α-PtO₂ layer formed on the surface. However, this layer became unstable above 750 K and changed into an oxide phase—PtO₃-Pt. PtO₃-Pt demonstrates exceptional thermal stability and endurance under high-temperature conditions.

Structural analyses and theoretical studies revealed the unique six-pointed star structure of PtO₃-Pt, critical in minimizing in-plane stress and promoting unidirectional domain nucleation. This leads to the epitaxial growth of large-area, single-crystal PtO₃-Pt. Theoretical models were crucial in understanding the key spectroscopic aspects of 2D PtO₃-Pt formation and confirming the structure and stability of this oxide. Additionally, this Pt oxide displays a distinctive surface electronic structure, which can selectively oxidize CO in mixed hydrocarbon, oxygen and CO environments (Supplementary Note 10). Moreover, the remarkable stability of PtO₃-Pt suggests that under high-temperature oxidizing conditions, the active phase of Pt is a 2D layered Pt oxide.

Our findings reveal that 2D PtO₃-Pt plays a crucial role not just as a transient phase but as a stable, active entity even above 700 K, which could revolutionize the design and application of Pt-based catalysts. The identification of a stable Pt oxide phase at these temperatures provides a perspective on catalyst behaviour under operating conditions typically considered detrimental to oxide stability. This discovery has profound implications for catalytic science, potentially leading to the development of more effective catalysts that leverage the unique properties of Pt oxides.

This research highlights the importance of using multiple in situ methods to get a comprehensive view of surface reactions from the atomic level to the millimetre scale, and bridges the gap between UHV techniques and real-world industrial conditions. Our methods and results not only deepen our understanding of surface oxidation but also open up new possibilities for designing high-temperature industrial catalysts.

Online content

Any methods, additional references, Nature Portfolio reporting summaries, source data, extended data, supplementary information, acknowledgements, peer review information; details of author contributions and competing interests; and statements of data and code availability are available at <https://doi.org/10.1038/s41563-024-02002-y>.

References

1. Tian, N., Zhou, Z.-Y., Sun, S.-G., Ding, Y. & Wang, Z. L. Synthesis of tetrahedral platinum nanocrystals with high-index facets and high electro-oxidation activity. *Science* **316**, 732–735 (2007).

2. Kašpar, J., Fornasiero, P. & Hickey, N. Automotive catalytic converters: current status and some perspectives. *Catal. Today* **77**, 419–449 (2003).
3. Chmielarz, L. & Jabłońska, M. Advances in selective catalytic oxidation of ammonia to dinitrogen: a review. *RSC Adv.* **5**, 43408–43431 (2015).
4. Park, S., Vohs, J. M. & Gorte, R. J. Direct oxidation of hydrocarbons in a solid-oxide fuel cell. *Nature* **404**, 265–267 (2000).
5. Jones, J. et al. Thermally stable single-atom platinum-on-ceria catalysts via atom trapping. *Science* **353**, 150–154 (2016).
6. Liu, J. et al. High performance platinum single atom electrocatalyst for oxygen reduction reaction. *Nat. Commun.* **8**, 15938 (2017).
7. Mom, R. et al. The oxidation of platinum under wet conditions observed by electrochemical X-ray photoelectron spectroscopy. *J. Am. Chem. Soc.* **141**, 6537–6544 (2019).
8. Ackermann, M. D. et al. Structure and reactivity of surface oxides on Pt(110) during catalytic CO oxidation. *Phys. Rev. Lett.* **95**, 255505 (2005).
9. Beniya, A. et al. CO oxidation activity of non-reducible oxide-supported mass-selected few-atom Pt single-clusters. *Nat. Commun.* **11**, 1888 (2020).
10. Chen, J. et al. Diversity of platinum-sites at platinum/fullerene interface accelerates alkaline hydrogen evolution. *Nat. Commun.* **14**, 1711 (2023).
11. Yu, F.-Y. et al. Pt-O bond as an active site superior to Pt₀ in hydrogen evolution reaction. *Nat. Commun.* **11**, 490 (2020).
12. Salmerón, M., Brewer, L. & Somorjai, G. A. The structure and stability of surface platinum oxide and of oxides of other noble metals. *Surf. Sci.* **112**, 207–228 (1981).
13. Saliba, N. A., Tsai, Y. L., Panja, C. & Koel, B. E. Oxidation of Pt(111) by ozone (O₃) under UHV conditions. *Surf. Sci.* **419**, 79–88 (1999).
14. Helveg, S. et al. Role of surface elastic relaxations in an O-induced nanopattern on Pt(110)–(1×2). *Phys. Rev. Lett.* **98**, 115501 (2007).
15. Devarajan, S. P., Hinojosa, J. A. & Weaver, J. F. STM study of high-coverage structures of atomic oxygen on Pt(111): p(2×1) and Pt oxide chain structures. *Surf. Sci.* **602**, 3116–3124 (2008).
16. Fantauzzi, D. et al. Growth of stable surface oxides on Pt(111) at near-ambient pressures. *Angew. Chem. Int. Ed.* **56**, 2594–2598 (2017).
17. Van Spronsen, M. A., Frenken, J. W. M. & Groot, I. M. N. Observing the oxidation of platinum. *Nat. Commun.* **8**, 429 (2017).
18. Salanov, A. N. et al. Oxidation and recrystallization of platinum group metals (Pt, Pd, Rh) in oxygen. Surface and subsurface reconstruction of polycrystalline platinum during annealing in the O₂ atmosphere over the temperature range of 600–1400 K. *Appl. Surf. Sci.* **490**, 188–203 (2019).
19. Steininger, H., Lehwald, S. & Ibach, H. Adsorption of oxygen on Pt(111). *Surf. Sci.* **123**, 1–17 (1982).
20. Weaver, J. F., Chen, J.-J. & Gerrard, A. L. Oxidation of Pt(111) by gas-phase oxygen atoms. *Surf. Sci.* **592**, 83–103 (2005).
21. Fryburg, G. C. Enhanced oxidation of platinum in activated oxygen. *J. Chem. Phys.* **24**, 175–180 (1956).
22. Krier, C. A. & Jaffee, R. I. Oxidation of the platinum-group metals. *J. Less-Common Met.* **5**, 411–431 (1963).
23. Ertl, G. Oscillatory kinetics and spatio-temporal self-organization in reactions at solid surfaces. *Science* **254**, 1750–1755 (1991).
24. Cirak, F. et al. Oscillatory thermomechanical instability of an ultrathin catalyst. *Science* **300**, 1932–1936 (2003).
25. Aitbekova, A. et al. Templated encapsulation of platinum-based catalysts promotes high-temperature stability to 1,100 °C. *Nat. Mater.* **21**, 1290–1297 (2022).
26. Tao, F. et al. Break-up of stepped platinum catalyst surfaces by high CO coverage. *Science* **327**, 850–853 (2010).
27. Wang, Z.-J. et al. The coalescence behavior of two-dimensional materials revealed by multiscale in situ imaging during chemical vapor deposition growth. *ACS Nano* **14**, 1902–1918 (2020).
28. Hansen, P. L. et al. Atom-resolved imaging of dynamic shape changes in supported copper nanocrystals. *Science* **295**, 2053–2055 (2002).
29. Cai, J. et al. Formation of different Rh–O species on Rh(110) and their reaction with CO. *ACS Catal.* **13**, 11–18 (2023).
30. Wang, Z.-J. et al. Conversion of chirality to twisting via sequential one-dimensional and two-dimensional growth of graphene spirals. *Nat. Mater.* **23**, 331–338 (2024).
31. Salmeron, M. & Schlögl, R. Ambient pressure photoelectron spectroscopy: a new tool for surface science and nanotechnology. *Surf. Sci. Rep.* **63**, 169–199 (2008).
32. Starr, D., Liu, Z., Hävecker, M., Knop-Gericke, A. & Bluhm, H. Investigation of solid/vapor interfaces using ambient pressure X-ray photoelectron spectroscopy. *Chem. Soc. Rev.* **42**, 5833–5857 (2013).
33. Cai, J. et al. An APXPS endstation for gas–solid and liquid–solid interface studies at SSRF. *Nucl. Sci. Tech.* **30**, 81 (2019).
34. Chaston, J. C. Reactions of oxygen with the platinum metals. *Platin. Met. Rev.* **9**, 51–56 (1965).
35. Plessow, P. N. & Abild-Pedersen, F. Sintering of Pt nanoparticles via volatile PtO₂: simulation and comparison with experiments. *ACS Catal.* **6**, 7098–7108 (2016).
36. Parkinson, C. R., Walker, M. & Mcconville, C. F. Reaction of atomic oxygen with a Pt(111) surface: chemical and structural determination using XPS, CAICISS and LEED. *Surf. Sci.* **545**, 19–33 (2003).
37. Zhu, J. F., Kinne, M., Fuhrmann, T., Denecke, R. & Steinrück, H. P. In situ high-resolution XPS studies on adsorption of NO on Pt(111). *Surf. Sci.* **529**, 384–396 (2003).
38. Miller, D. J. et al. Oxidation of Pt(111) under near-ambient conditions. *Phys. Rev. Lett.* **107**, 195502 (2011).
39. Li, X. et al. Single-crystal two-dimensional material epitaxy on tailored non-single-crystal substrates. *Nat. Commun.* **13**, 1773 (2022).
40. Sutter, P. How silicon leaves the scene. *Nat. Mater.* **8**, 171–172 (2009).
41. Wang, L. et al. Epitaxial growth of a 100-square-centimetre single-crystal hexagonal boron nitride monolayer on copper. *Nature* **570**, 91–95 (2019).
42. Sutter, P. W., Flege, J.-I. & Sutter, E. A. Epitaxial graphene on ruthenium. *Nat. Mater.* **7**, 406–411 (2008).
43. Wang, Z.-J. et al. Formation mechanism, growth kinetics and stability limits of graphene adlayers in metal-catalyzed CVD growth. *Adv. Mater. Interfaces* **5**, 1800255 (2018).
44. Hu, P. & King, D. A. A direct inversion method for surface structure determination from LEED intensities. *Nature* **360**, 655–658 (1992).
45. Gustafson, J. et al. Self-limited growth of a thin oxide layer on Rh(111). *Phys. Rev. Lett.* **92**, 126102 (2004).
46. Lundgren, E. et al. Two-dimensional oxide on Pd(111). *Phys. Rev. Lett.* **88**, 246103 (2002).
47. Krasnikov, S. A. et al. Self-limited growth of triangular PtO₂ nanoclusters on the Pt(111) surface. *Nanotechnology* **21**, 335301 (2010).
48. Huang, B. et al. Layer-dependent ferromagnetism in a van der Waals crystal down to the monolayer limit. *Nature* **546**, 270–273 (2017).
49. Nair, S. et al. Engineering metal oxidation using epitaxial strain. *Nat. Nanotechnol.* **18**, 1005–1011 (2023).
50. Gao, M.-R. et al. Completely green synthesis of colloid Adams’ catalyst α-PtO₂ nanocrystals and derivative Pt nanocrystals with high activity and stability for oxygen reduction. *Chem. Eur. J.* **18**, 8423–8429 (2012).

51. Tang, M. et al. Recent progresses on structural reconstruction of nanosized metal catalysts via controlled-atmosphere transmission electron microscopy: a review. *ACS Catal.* **10**, 14419–14450 (2020).
52. Salmeron, M. & Eren, B. High-pressure scanning tunneling microscopy. *Chem. Rev.* **121**, 962–1006 (2021).
53. Alcock, C. B., Hooper, G. W. & Nyholm, R. S. Thermodynamics of the gaseous oxides of the platinum-group metals. *Proc. R. Soc. Lond. A* **254**, 551–561 (1960).
54. Xiong, H. et al. Metastable Pd↔PdO structures during high temperature methane oxidation. *Catal. Lett.* **147**, 1095–1103 (2017).
55. Xiong, H. et al. Engineering catalyst supports to stabilize PdO_x two-dimensional rafts for water-tolerant methane oxidation. *Nat. Catal.* **4**, 830–839 (2021).

Publisher's note Springer Nature remains neutral with regard to jurisdictional claims in published maps and institutional affiliations.

Open Access This article is licensed under a Creative Commons Attribution-NonCommercial-NoDerivatives 4.0 International License, which permits any non-commercial use, sharing, distribution and reproduction in any medium or format, as long as you give appropriate credit to the original author(s) and the source, provide a link to the Creative Commons licence, and indicate if you modified the licensed material. You do not have permission under this licence to share adapted material derived from this article or parts of it. The images or other third party material in this article are included in the article's Creative Commons licence, unless indicated otherwise in a credit line to the material. If material is not included in the article's Creative Commons licence and your intended use is not permitted by statutory regulation or exceeds the permitted use, you will need to obtain permission directly from the copyright holder. To view a copy of this licence, visit <http://creativecommons.org/licenses/by-nc-nd/4.0/>.

© The Author(s) 2024

Methods

The Pt(111) single crystal was purchased from MaTeck. The gas lines for NO₂ were baked at 120 °C for 24 h and flushed several times using high-purity NO₂ (99.995%) before introducing NO₂ into the chamber to minimize contamination.

In situ SEM

The in situ observational experiments were conducted within the confines of a chamber in a specially modified commercial ESEM instrument (Thermo Fisher Quattro S). The vacuum system of the ESEM instrument utilized oil-free pre-vacuum pumps. A custom-made laser-heating stage was incorporated into the instrument, in addition to a gas supply module facilitated by mass flow controllers from Bronkhorst, and a mass spectrometer (Pfeiffer HiQuad) was used for atmospheric analysis within the chamber. The ESEM chamber was subjected to a thorough cleaning process using plasma before the experiments. Temperature was determined using a K-type thermocouple, which was meticulously spot-welded onto the substrate. The microscope operation was maintained at an acceleration voltage ranging from 2 kV. A large field detector was utilized for image capture. Throughout the experiments, no influence of the electron beam on the oxidation process was detected.

In situ XPS

In situ XPS measurements were performed utilizing the advanced synchrotron-based AP-XPS system located at beamline O2B01 of the Shanghai Synchrotron Radiation Facility. Additionally, a complementary laboratory-based SPECS AP-XPS system was used. Both systems were outfitted with high-transmission analysers, integrated with a preparation chamber and a μ -metal main chamber maintained at a base pressure of 1×10^{-9} mbar. The synchrotron-based AP-XPS system is capable of achieving an energy resolution of up to 13,000, with a focused beam spot size of approximately 460 μm (horizontal) \times 15 μm (vertical). The laboratory-based AP-XPS system features a spot size of roughly 300 μm in diameter. Sample temperatures were precisely controlled within the range of 300–1,000 K using an infrared laser-heating unit. A mass spectrometer, connected to the first differential pumping stage, was used for the real-time monitoring of gas-phase components within the analysis chamber.

To mitigate issues related to carbon segregation from the bulk, the Pt(111) single crystal was subjected to an iterative cleaning procedure involving Ar⁺ sputtering (15 min, 1 keV) followed by annealing at 700 °C for 10 min. This process effectively removed the dissolved carbon and other surface contaminants, resulting in a pristine Pt(111) surface.

Unless specified otherwise, spectral analysis was conducted using CasaXPS software (Version 2.3.25PRL0) with a Shirley-type background correction (<https://doi.org/10.1016/j.apsadv.2021.100112>). The O1s spectra were fitted with a GL(30) line shape, representing a mixture of 70% Gaussian and 30% Lorentzian components, and the asymmetric Pt4f spectra were fitted using a DS(0.02,100)GL(30) line shape, which combines Doniach–Sunjic asymmetry with a Gaussian–Lorentzian (product) function.

EBSD

EBSD patterns were obtained using an EDAX Velocity Super EBSD detector on a Thermo Fisher ApreoSEM instrument. The analysis, encompassing phase identification and orientation-map generation, was performed using EDAX's OIM Analysis 8 software (Version: 8.6.108x64).

Quasi-in situ STM

Quasi-in situ STM experiments were conducted using SPECS JT-STM, a commercial STM system. For these experiments, the sample was transported to the STM setup via a UHV transfer suitcase. After loading into the STM chamber, the sample was transferred to a cryogenic stage and maintained at 5 K to ensure optimal imaging conditions. The commercial Pt–Ir tip, utilized for both imaging and tunnelling, had

been previously calibrated on silver islands formed on p-type Si(111) surfaces with a 7×7 reconstruction.

In situ TEM

Pt particles (ADAMAS-BETA) were dispersed in pure ethanol. The mixture was then drop-cast onto a commercial microelectromechanical system chip (Protochips) followed by drying in air. A closed cell with electron-transparent SiN_x window and heating device were assembled on an in situ transmission electron microscopy (TEM) holder. An electrical current was applied through the gold contacts to the SiC heating membrane. Using an external gas-feeding system, the in situ observations were conducted under the flowing-gas mode. An integrated residual gas analyser was used to verify the gas mixture applied to the cell. The observation was conducted in an aberration-corrected JEM Grand ARM 300F TEM instrument (JEOL) operated in the scanning mode (STEM) at 300 kV. The microscope is equipped with high-angle annular dark-field STEM detector. In situ observations of Pt oxidation were made at various temperatures from 300 to 1,000 K in a flowing NO₂ gas environment (0.1 bar, 0.12 s.c.c.m.). Due to the large temperature span for investigation, a single-particle observation was impossible as a result of sample rotation and the tilt-off of the appropriate zone axis. Therefore, multilocation assessments were applied to obtain the surface-layer structure with Pt-[111] atomic arrangement.

In high-angle annular dark-field STEM imaging mode, the electron signal is mainly derived from the Rutherford scattering of incoherent electrons. Due to this, it is not expected that any phase contrast from the edge of the particle, as well as the atomic arrangements of Pt, can be well interpreted by the high-angle annular dark-field intensity distribution. Additionally, the mass-thickness contrast (particularly Z contrast) is promoted for Pt through the avoidance of the O-lattice Bragg scattering at low angles. In particular, the O intensity is suppressed (therefore, no O atom can be 'seen') in this mode to facilitate a clear interpretation of atomic locations for Pt. On the basis of this, we carefully examine the atomic location for the Pt overlayer with respect to the bulk Pt atoms (Fig. 5c). The imaged atomic position demonstrates reasonable agreement with the simulated result (Fig. 5c, inset), despite a slightly compromised resolution at elevated temperature (1,000 K). A spatial filter of 5×5 convolution is applied to the original image to enhance the contrast of Pt atoms (both images are shown in Supplementary Fig. 17).

EELS

Environmental STEM analysis of the Pt(111) surface was conducted using Hitachi HF5000, an aberration-corrected microscope, operated at 200 kV. To prepare a clean Pt(111) surface, Pt particles were dispersed on a microelectromechanical system chip and subsequently treated in 1 Pa H₂ at temperatures above 600 °C for 3 h. The temperature was then increased to 700 °C, and NO₂ was introduced at a flow rate of 1.5 ml min⁻¹ for a total of 75 ml for subsequent analyses. Annular dark-field imaging was carried out under standard dose rates, and no beam-induced damage was detected. Elemental analysis of the Pt(111) surface was performed using EELS line scan in HF5000, equipped with a Gatan 965 EELS spectrometer. The EELS spectra were collected in the range of 300–812 eV, with a dispersion setting of 0.25 eV per channel.

Calculation details

DFT calculation. DFT calculations were performed using the Vienna ab initio simulation package code^{56,57}. The Perdew–Burke–Ernzerhof exchange–correlation functional was used to set the plane-wave basis, and the cutoff energy was set to 380 eV (ref. 58). The Brillouin zone was sampled using a Monkhorst–Pack $1 \times 1 \times 1$ *k*-point grid, and the wavefunction was converged to 1×10^{-4} eV. The DFT-D3 method of Grimme was applied to account for the van der Waals interactions⁵⁹. Structure optimizations were performed with on-the-fly machine learning force field implemented using the Vienna ab initio simulation package software, which has been shown to accurately predict the DFT data⁶⁰.

MD simulation. MD simulations were carried out in LAMMPS package with LASP machine learning force field in a constant volume and constant temperature (*NVT*) system^{61,62}. The MD simulations were performed for 10 ps with a time step of 1 fs. The Pt substrate was fixed, and PtO_x was allowed to move during structure optimizations and MD simulations.

XPS/STM simulation and molecular orbital analysis. The STM image of the surfaces was calculated and analysed in the Vienna ab initio simulation package (https://www.vasp.at/wiki/index.php/STM_of_graphene).

The XPS simulations were performed by calculating the core-level binding energy changes with the final-state approximation. In this approximation, the core-level binding energies were calculated following the procedure described elsewhere^{63,64}.

The wavefunction plots were drawn with the help of the VASPMO (<https://sourceforge.net/projects/vaspmo/>) and Molekel (<http://ugovaretto.github.io/molekel/>) programs.

A simplified system was modelled in the XPS/STM simulation and molecular orbital analysis. The system was modelled using a Pt substrate on a periodic 2 × 3 Pt(111) slab with two atomic layers. Then, a PtO₃-Pt layer with 4 Pt and 12 O atoms were placed in the vacuum layer above the Pt substrate. The lattice of the system was 8.316 × 4.8 × 30 Å³, and the Brillouin zone was sampled using a Monkhorst-Pack 2 × 4 × 1 *k*-point grid. Structure optimization was performed before the XPS/STM simulation and molecular orbital analysis.

Data availability

The data that support the findings of this study are available from the corresponding authors on reasonable request. Source data are provided with this paper.

References

- Hafner, J. Ab-initio simulations of materials using VASP: density-functional theory and beyond. *J. Comput. Chem.* **29**, 2044–2078 (2008).
- Kresse, G. & Hafner, J. Ab initio molecular dynamics for open-shell transition metals. *Phys. Rev. B* **48**, 13115–13118 (1993).
- Perdew, J. P. et al. Atoms, molecules, solids and surfaces: applications of the generalized gradient approximation for exchange and correlation. *Phys. Rev. B* **46**, 6671–6687 (1992).
- Grimme, S., Antony, J., Ehrlich, S. & Krieg, H. A consistent and accurate ab initio parametrization of density functional dispersion correction (DFT-D) for the 94 elements H-Pu. *J. Chem. Phys.* **132**, 154104 (2010).
- Jinnouchi, R., Karsai, F. & Kresse, G. On-the-fly machine learning force field generation: application to melting points. *Phys. Rev. B* **100**, 014105 (2019).
- Huang, S.-D., Shang, C., Kang, P.-L., Zhang, X.-J. & Liu, Z.-P. LASP: fast global potential energy surface exploration. *WIREs Comput. Mol. Sci.* **9**, e1415 (2019).
- Thompson, A. P. et al. LAMMPS—a flexible simulation tool for particle-based materials modeling at the atomic, meso and continuum scales. *Comput. Phys. Commun.* **271**, 108171 (2023).
- Köhler, L. & Kresse, G. Density functional study of CO on Rh(111). *Phys. Rev. B* **70**, 165405 (2004).

- Zeng, Z., Ma, X., Ding, W. & Li, W.-X. First-principles calculation of core-level binding energy shift in surface chemical processes. *Sci. China Chem.* **53**, 402–410 (2010).

Acknowledgements

This work was mainly supported by the National Natural Science Foundation of China under grant no. 12027804. Zhi Liu acknowledges the Science and Technology Commission of Shanghai Municipality (no. 22560780300). This work was supported by the National Key R&D Program of China (no. 2022YFA1503802) and the National Natural Science Foundation of China (nos. 21991152, 22002090, 21902179 and 52025023). J.C. and Z.-J.W. thank BL02B01 of the Shanghai Synchrotron Radiation Facility and SPECS AP-XPS instrument supported by the National Natural Science Foundation of China (no. 11227902). J.C. and Z.-J.W. acknowledge X. Kong from the Shanghai Institute of Microsystem and Information Technology for the theoretical simulation. B.Y. acknowledges funding support from the National Natural Science Foundation of China (22322302). We also thank the HPC Platform of ShanghaiTech University for computing time. We acknowledge the Center for High-Resolution Electron Microscopy of ShanghaiTech University for use of the electron microscope. K.L. acknowledges Guangdong Major Project of Basic and Applied Basic Research (2021B0301030002).

Author contributions

Z.-J.W. conceived this project and supervised the research. In situ SEM and EBSD experiments and analysis were conducted by Z.-J.W., J.C., C.X. and M.-G.W. AP-XPS and LEED experiments and analysis were performed by J.C., Y.Z., H.Z., Z.-J.W. and Zhi Liu. Quasi-in situ STM measurements and analysis were performed by L.W., J.C., M.W., Z.-J.W. and Zhongkai Liu. The in situ TEM, high-angle annular dark-field STEM and EELS measurements were performed by Z.C., Y.H., J.C., T.Q., L.C. and X.L. The theoretical simulations and implementation of the obtained results were carried out by J.L., W.S., B.Y., K.L. and P.H. Important contributions to the interpretation of the results, conception and writing of the paper were made by J.C. and Z.-J.W. All authors participated in the scientific discussion.

Competing interests

The authors declare no competing interests.

Additional information

Supplementary information The online version contains supplementary material available at <https://doi.org/10.1038/s41563-024-02002-y>.

Correspondence and requests for materials should be addressed to Bo Yang, Zhongkai Liu, Zhi Liu or Zhu-Jun Wang.

Peer review information *Nature Materials* thanks Matteo Cargnello, Abhaya Datye and Jakob Wagner for their contribution to the peer review of this work.

Reprints and permissions information is available at www.nature.com/reprints.